*Chemical Engineering & Technology*

Chemical & Engineering Technology

RESEARCH ARTICLE OPEN ACCESS

# Influence of Particle Aspect Ratio on Translational Collision Dynamics in Wall-Bounded Turbulence

Connor H. Nolan[1] | Lee F. Mortimer[2] | Peter K. Jimack[3] | Michael Fairweather[2]

[1]University of Leeds, Leeds, UK | [2]School of Chemical and Process Engineering, University of Leeds, Leeds, UK | [3]School of Computer Science, University of Leeds, Leeds, UK

**Correspondence:** Connor H. Nolan (mm18cn@leeds.ac.uk)

**Received:** 30 November 2025 | **Revised:** 31 May 2026 | **Accepted:** 2 June 2026

**Keywords:** collision dynamics | four-way coupling | Lagrangian particle tracking | non-spherical particles

## ABSTRACT

This study examines how particle shape influences collision dynamics in turbulent channel flow using direct numerical simulation (DNS) with Lagrangian tracking and fully resolved four-way coupling. Rigid ellipsoids across aspect ratios are simulated with inertia-driven translation, hydrodynamic forces, and quaternion-based rotation. Needle-like particles align more strongly with the local shear, reducing turbulent scattering and producing lower collision velocities with narrower angle distributions. Nearly spherical particles respond more intensely to turbulence, yielding broader collision statistics. Some features, such as spanwise velocity fluctuations, remain largely shape-independent, highlighting the dominance of lateral turbulent motions.

## 1 | Introduction

Particle-laden flows occur widely in both natural environments and industrial processes, from the development of riverbeds [1] to the transport of nuclear waste [2]. In many such systems, small, dense particles collide frequently. In many cases, these particles are non-spherical, for example, in papermaking [3] or within clouds [4]. Understanding both the particle-scale and bulk-scale dynamics of such flows is essential for predicting large-scale phenomena, such as dispersion, deposition, turbulence modulation, and clogging. This knowledge allows for the optimization of processes and ensuring the safety and reliability of new technologies.

In recent years, advances in computational performance have allowed direct numerical simulation (DNS) and Lagrangian particle tracking (LPT) methodologies to aid the prediction of particle-laden flows at industrially relevant particle inertia and solid-phase volume fraction. These tools have successfully reproduced many bulk behaviors reported experimentally, including turbophoresis and preferential concentration [5]. In fact, modern computational fluid dynamics can now resolve particle-scale interactions with a level of detail that often exceeds what is achievable experimentally. As such, first-principles approaches, particularly DNS, which resolves spatial and temporal scales down to the Kolmogorov length scale [6], remain indispensable for accurately studying key physical phenomena. Comprehensive overviews of recent advances in particle-laden turbulent flows, including developments in DNS, LPT methodologies, particle–turbulence interaction mechanisms, and modeling challenges across coupling regimes, are provided by [7].

It should be noted that the present study employs a point-particle (sub-grid) approach, where the ellipsoidal particles are tracked in a Lagrangian framework and coupled to the fluid via point-force correlations. This approach is computationally efficient for high particle counts but relies on established closure models for the hydrodynamic forces, such as the drag and lift forces. Although this work focuses on point-particle LPT, an alternative approach is the use of fully resolved simulations (FRS), where the flow around each individual particle is explicitly resolved on the numerical grid [8]. Such methods provide high-fidelity data on the torque and stress distributions across a non-spherical particle's surface, which can sometimes reveal deviations from point-particle predictions, particularly regarding wake effects and particle-turbulence modulation in the dense regime [9]. However, due to the high computational cost of resolving thousands of non-spherical particles, FRS remain outside the scope of this investigation.

Significant contributions have been made in the study of spherical particle-laden turbulent flows at low-volume fractions ($\phi_p \leq 10^{-6}$) where one-way coupling is sufficient and particles do not influence the carrier flow. These studies have clarified the mechanisms governing particle migration, such as preferential concentration and turbophoresis. Preferential concentration is strongest at moderate Stokes numbers, where particles cluster within low-speed streaks and near-wall regions [10]. Turbophoresis describes the tendency of particles to move towards areas with lower-than-average turbulence kinetic energy and has been shown to scale with the particle Stokes number across the moderate range [11]. Extensive research on near-wall dynamics has revealed diverse particle behaviours arising from different material properties and inertia [12]. The dynamics, both translational and rotational, of non-spherical ellipsoidal particles has also been studied using one-way coupled LPT simulations. However, the majority of such studies focus exclusively on prolate ellipsoids with aspect ratios $\lambda > 1$, often referred to in the literature as fibers. These works report that aspect ratio has a limited influence on clustering, preferential concentration, or segregation [13] but strongly affects near-wall behavior with longer fibers depositing more readily and showing strong alignment with the streamwise direction, with this weakening as inertia increases. The broader implications of particle anisotropy for dispersion, alignment, and rotational dynamics in both homogeneous and wall-bounded turbulence are extensively discussed by Voth and Soldati [14], who highlight how shape fundamentally alters particle–flow coupling mechanisms.

As the particle volume fraction increases ($10^{-6} \leq \phi_p \leq 10^{-3}$), the feedback of particles on the fluid becomes non-negligible, requiring two-way coupling. This is commonly implemented via momentum exchange between the particles and the fluid [15]. Studies of wall-bounded turbulence show that large particles enhance turbulence, whereas small particles dampen it. Interestingly, this trend diminishes at low particle-to-fluid density ratios, even when the Stokes numbers are matched. At increased Stokes numbers, inertial particles respond sluggishly to rapid flow variations and preferentially accumulate in low-turbulence regions, suppressing local turbulent activity and disrupting energy transfer across scales [6].

As the volume fraction increases further, to around $\phi_p > 10^{-3}$, the translational and rotational motion of the particle begins to be affected by inter-particle collisions which at this point occur very frequently. It is therefore necessary for simulations to be able to detect and resolve such collisions which is computationally expensive, especially in the case of non-spherical particles. Collision-dominated particle-laden turbulence has been widely explored; for example, one study found that low-Stokes number particles favor regions of irrotational dissipation, and that relative collision velocity increases with Reynolds number [16]. Four-way-coupled LPT simulations of vertical channel flows have shown that even microparticles at very low volume fractions ($\phi_p \approx 10^{-5}$) can significantly modify turbulence due to the high frequency of collisions [17]. Although some studies have incorporated four-way coupling and non-sphericity, quantitative analysis of how particle shape influences collision dynamics remains limited. Existing work suggests that ellipsoids collide more frequently, and with higher relative velocities, than spheres of equal volume [18]. For high-inertia particles, collisions strongly alter momentum transfer and slip-velocity orientation, making four-way coupling essential at intermediate Stokes numbers [5].

A range of collision-detection strategies have been developed, including neighbor-list approaches and stochastic models. In the present work, we employ a deterministic, partition-based scheme [19] combined with a hard-sphere collision model. More advanced algorithms for non-spherical particles approximate particle volumes using assemblies of overlapping fictitious spheres [20], thus allowing collision handling to follow procedures like those used for spherical particles.

Few studies have examined particle-laden turbulence under the combined conditions of high particle inertia, non-sphericity, and fully resolved four-way coupling. In this work, we conduct simulations at comparatively high-particle loadings that capture these effects simultaneously, enabling a detailed investigation of shape-dependent collision dynamics and the mechanisms governing momentum and orientation exchange during turbulent interactions.

This study aims to deepen understanding of collision-driven dynamics in wall-bounded, particle-laden turbulent channel flows, with a particular emphasis on the roles of particle non-sphericity and high inertia. Ultimately, our goal is to provide mechanistic insight and to generate collision statistics within well-validated canonical turbulent channel flow.

## 2 | Methodology

### 2.1 | Fluid Phase Modeling

To obtain fully resolved predictions of the carrier-phase flow, we employ the spectral element DNS solver Nek5000 [21]. The code uses seventh-order polynomial approximations within each element and is well suited for the present study due to its open-source flexibility, efficient parallel scalability, and extensive validation record. We simulate a turbulent channel flow at a shear Reynolds number $Re_\tau = u_\tau \delta / \nu_F = 300$, where $u_\tau$ is the shear velocity, $\delta$ is the half channel height and $\nu_F$ is the fluid kinematic viscosity. Although higher Reynolds numbers are encountered in industrial applications, this canonical value is selected to provide a well-resolved turbulent channel flow that allows for a controlled, fundamental investigation into the effects of particle morphology on collision statistics without excessive computational cost. The dynamics of the continuous phase are governed by the incompressible Navier–Stokes equations, expressed in non-dimensional form as

$$\nabla \cdot \mathbf{u}_F^* = 0, \tag{1}$$


**FIGURE 1** | Computational mesh demonstrating element spacings and increased near-wall nodal density. The size of the domain is specified in terms of the characteristic length scale $\delta = 0.02$ m, the half channel height.

$$\frac{D\mathbf{u}_F^*}{Dt^*} = -\nabla p^* + \frac{1}{Re_B}\nabla^2\mathbf{u}_F^* + \mathbf{f}_{\mathrm{PG}}^* + \mathbf{f}_{2W}^*, \tag{2}$$

where $\mathbf{u}_F^*(\mathbf{x}^*, t^*)$ is the fluid velocity vector at position $\mathbf{x^*}$ and time $t^*$, $p^*(\mathbf{x^*},t^*)$ is the fluid pressure, $Re_B = u_B\,\delta/\nu_F$ is the bulk Reynolds number, $\mathbf{f}_{\mathrm{PG}}^*$ is a constant pressure gradient forcing term and $\mathbf{f}_{2W}^*$ is an arbitrary cell-dependent forcing term accounting for two-way momentum exchange between the particles and the fluid. Parameters marked with an asterisk (*) signify a non-dimensional variable obtained from the bulk properties ($\delta$, $u_B$, $\rho_F$), where $\rho_F$ is the density of the fluid.

The computational domain is discretized using a structured mesh comprising 27 × 18 × 23 spectral elements (approximately 3.9 million grid points). Element spacing is refined in the wall-normal direction and is uniform in the streamwise and spanwise directions. The coordinate directions $x$, $y$, and $z$ correspond to the streamwise, wall-normal, and spanwise axes, respectively. The domain and associated mesh are shown in Figure 1. A constant time step of $\Delta t^* = 0.0025$ is used for both the fluid and particle solvers. This value is chosen such that both translation and rotation are fully resolved and that collisions are well handled. Periodic boundary conditions are applied in the streamwise and spanwise directions, whereas no-slip and impermeability conditions are imposed at the walls located at $y^* = \pm 1$. The channel flow is driven by a constant pressure gradient in the streamwise direction chosen to achieve the desired Reynolds number, with magnitude:

$$\frac{dp^*}{dx^*} = \left(\frac{Re_\tau}{Re_B}\right)^2. \tag{3}$$

## 2.2 | Lagrangian Particle Tracking

Particle trajectories and orientations are computed using a Lagrangian particle-tracking framework developed to run in parallel with Nek5000. Each particle is treated as a point mass whose position, velocity, orientation (via quaternions), and angular velocity are updated every time step by integrating a set of non-dimensional equations of motion. The translational dynamics are obtained from the balance between the particle inertia and the hydrodynamic forces exerted by the carrier fluid. The model accounts for drag, lift, virtual mass, and pressure-gradient forces. The Basset history force is omitted due to its high computational cost and limited influence under the present flow conditions. Gravity and buoyancy are also neglected to isolate turbulence–particle interactions.

For rotational motion, particle orientation is represented by quaternions, and angular velocities are updated using Euler's equations for rigid-body rotation. The torques considered include those arising from viscous resistance on a rotating ellipsoid and the coupling between angular motion about different axes associated with unequal principal moments of inertia.

### 2.2.1 | Geometry of the Non-Spherical Particles

The particles are prolate ellipsoids defined by

$$\left(\frac{x'}{a}\right)^2 + \left(\frac{y'}{b}\right)^2 + \left(\frac{z'}{c}\right)^2 = 1, \tag{4}$$

where $a$, $b$, and $c$ are the semi-principal axes along the particle frame axes $x'$, $y'$, $z'$, respectively. Throughout this work, we impose $a = b$ and define the aspect ratio as $\lambda = c/a$. The solid phase is characterized by the particle density $\rho_p$, aspect ratio $\lambda$, and the volume fraction:

$$\phi_p = \frac{4}{3}\pi a^2 c\frac{N_p}{V_F}, \tag{5}$$

where $N_p$ is the number of particles and $V_F$ is the fluid domain volume.

Three coordinate systems are employed: the particle-fixed frame $\mathbf{x'}$, centred at the particle centroid; the global frame $\mathbf{x}$; and a co-moving frame $\mathbf{x''}$ that shares the particle centroid but remains aligned with the global axes. Transformations between $\mathbf{x'}$and $\mathbf{x''}$ use the rotational matrix:

$$\mathbf{x}' = \underline{\underline{\mathbf{A}}}\mathbf{x}'' \tag{6}$$

where $\underline{\underline{\mathbf{A}}}$ is a time-dependent quaternion-derived rotation matrix, with quaternion components $\mathbf{q} = [q_0,q_1,q_2,q_3]^{\mathrm{T}}$ satisfying $q_0^2 + q_1^2 + q_2^2 + q_3^2 = 1$. The explicit form of $\mathbf{A}$ is given by the following equation:

$$\underline{\underline{\mathbf{A}}} = \begin{bmatrix} 1-2(q_2^2+q_3^2) & 2(q_1q_2+q_0q_3) & 2(q_1q_3-q_0q_2) \\ 2(q_1q_2-q_0q_3) & 1-2(q_1^2+q_3^2) & 2(q_2q_3+q_0q_1) \\ 2(q_1q_3+q_0q_2) & 2(q_2q_3-q_0q_1) & 1-2(q_1^2+q_2^2) \end{bmatrix} \tag{7}$$

The rotation matrix in Equation (7) follows a passive rotation convention, mapping vectors from the global frame to the particle-fixed frame. The quaternion evolution is governed by

$$\frac{d\mathbf{q}}{dt^*} = \frac{1}{2}\begin{bmatrix} q_0 & -q_1 & -q_2 & -q_3 \\ q_1 & q_0 & -q_3 & q_2 \\ q_2 & q_3 & q_0 & -q_1 \\ q_3 & -q_2 & q_1 & q_0 \end{bmatrix}\begin{bmatrix} 0 \\ \Omega_{x'} \\ \Omega_{y'} \\ \Omega_{z'} \end{bmatrix}, \tag{8}$$

where $\Omega_{x'}$,$\Omega_{y'}$,$\Omega_{z'}$ are the angular velocity components in the particle frame.

#### 2.2.2 | Translational Motion

The particle translational motion satisfies

$$\frac{d\boldsymbol{x}_p^*}{dt^*} = \mathbf{u}_p^*, \tag{9}$$

$$\frac{\partial \boldsymbol{u}_p^*}{\partial t^*} = \frac{1}{M_{\mathrm{VM}}}\left[\mathbf{F}_D + \mathbf{F}_L + \mathbf{F}_{\mathrm{VM}} + \mathbf{F}_{\mathrm{PG}}\right], \tag{10}$$

where $M_{\mathrm{VM}} = (1 + 1/2\rho^*)$ is the non-dimensional virtual mass factor and $\rho^* = \rho_p/\rho_F$. The drag force is

$$\mathbf{F}_D = \frac{A_D^* C_D\, |\mathbf{u}_s^*|\, \mathbf{u}_s^*}{2\rho^* V_p^*}, \tag{11}$$

where $V_p^* = (4/3)\pi a^{*2} c^*$ and $\mathbf{u}_s^* = \mathbf{u}_F^* - \mathbf{u}_p^*$ is the slip velocity. The projected areas associated with drag and lift are as follows [22]:

$$A_D = \pi a^2 \sqrt{\cos^2(\alpha) + \left(\frac{4\lambda}{\pi}\right)^2 \sin^2(\alpha)}, \tag{12}$$

$$A_L = \pi a^2 \sqrt{\sin^2(\alpha) + \left(\frac{4\lambda}{\pi}\right)^2 \cos^2(\alpha)}, \tag{13}$$

where $\alpha$ is the angle of incidence defined as the angle between the slip velocity $\mathbf{u}_s^*$ and the direction of the principal particle axis $\mathbf{z}'$.

The dimensionless drag coefficient $C_D$ for non-spherical particles is calculated using the correlation proposed by Ganser [23]. The drag coefficient is dependent upon the projected area $A_D$ and is therefore orientation-dependent through its sensitivity to the angle of incidence $\alpha$. The correlation is expressed as

$$\frac{C_D}{K_2} = \frac{24}{Re_p K_1 K_2}\left[1 + 0.118\left(Re_p K_1 K_2\right)^{0.6567}\right] + \frac{0.4305}{1 + 3305/\left(Re_p K_1 K_2\right)}, \tag{14}$$

where $Re_p = \mathbf{u}_s^*\, d_{\mathrm{ev}}/\nu_F$ is the particle Reynolds number computed using the equal volume sphere diameter $d_{\mathrm{ev}} = 2a\lambda^{1/3}$, $K_1 = \frac{1}{3}\left(d_n/d_{\mathrm{ev}} + 2\Phi_s^{-0.5}\right)$ and $K_2 = 10^{1.8148(-\log\Phi_s)^{0.5743}}$ are the Stokes and Newton shape factors that model the particle sphericity and orientation, respectively, $d_n = \sqrt{4A_D/\pi}$ and $\Phi_s = s/S$, where $\Phi_s$ is the particle sphericity, defined as the ratio of the surface area of a sphere having the same volume as the particle, $s$, to the actual surface area of the non-spherical particle, $S$.

The use of this orientation-dependent, projected-area-based formulation enables the simulation of a continuous range of aspect ratios, encompassing both prolate and oblate ellipsoids, without requiring geometry-specific recalibration or additional particle-resolved DNS data. In contrast, correlations, such as those proposed by Zastawny et al. [24], Ouchene et al. [25], and Chéron et al. [26], are derived for specific particle geometries and calibrated over restricted parameter ranges.

For the low particle Reynolds numbers considered in the present work ($Re_p \approx 1$), comparison with published DNS data for prolate ellipsoids at similar aspect ratios shows that the projected-area-based Ganser [23] formulation yields average absolute errors comparable to, and in some cases lower than, geometry-specific correlations (for further details see Appendix A). This demonstrates that, within the particle Reynolds number and aspect ratio ranges relevant to this study, the projected-area-based model provides sufficient accuracy while retaining broader applicability than the alternative correlations noted above.

The lift coefficient satisfies [22]:

$$\frac{|C_L|}{|C_D|} = \left|\sin^2(\alpha)\cos^2(\alpha)\right|, \tag{15}$$

and the lift force is [22]

$$\mathbf{F}_L = \frac{1}{2\rho^* V_p^*} A_L^* C_L \frac{(\mathbf{z}' \cdot \mathbf{u}_s^*)}{|\mathbf{u}_s^*|}\left[\mathbf{z}' \times \mathbf{u}_s^*\right] \times \mathbf{u}_s^* \tag{16}$$

The pressure-gradient and virtual mass forces are as follows [5]:

$$\mathbf{F}_{\mathrm{PG}} = \frac{1}{\rho^*}\frac{D\mathbf{u}_F^*}{Dt^*}, \tag{17}$$

$$\mathbf{F}_{\mathrm{VM}} = \frac{1}{2\rho^*}\frac{D\mathbf{u}_F^*}{Dt^*}. \tag{18}$$

The translational equations of motion (Equation 10) include the pressure-gradient and virtual mass forces for physical completeness, noting that these specific closures were originally derived for spherical particles. Computation of the lift coefficient in Equation (15) is adapted for non-spherical geometries using an analytical trigonometric relationship dependent on the angle of incidence. Although it is recognized that such point-particle correlations may lose accuracy under conditions of flow separation at high angles of incidence or complex wake interactions (phenomena not fully resolved in the LPT framework), the high particle-to-fluid density ratio ensures that these auxiliary forces remain secondary to drag and particle inertia.

#### 2.2.3 | Rotational Motion

$$\begin{aligned}
\frac{d\Omega_{x'}^*}{dt^*} &= \frac{20\left[(1-\lambda^2)d_{z'y'}^* + (1+\lambda^2)(\omega_{z'y'}^* - \Omega_{x'}^*)\right]}{Re_B(\beta_0 + \lambda^2\gamma_0)(1+\lambda^2)\rho^* a^{*2}} + \left(1 - \frac{2}{1+\lambda^2}\right)\Omega_{y'}^*\Omega_{z'}^*, \\
\frac{d\Omega_{y'}^*}{dt^*} &= \frac{20\left[(\lambda^2-1)d_{x'z'}^* + (\lambda^2+1)(\omega_{x'z'}^* - \Omega_{y'}^*)\right]}{Re_B(\alpha_0 + \lambda^2\gamma_0)(1+\lambda^2)\rho^* a^{*2}} + \left(\frac{2}{1+\lambda^2} - 1\right)\Omega_{x'}^*\Omega_{z'}^*, \\
\frac{d\Omega_{z'}^*}{dt^*} &= \frac{20\left(\omega_{y'x'}^* - \Omega_{z'}^*\right)}{Re_B(2\alpha_0)\rho^* a^{*2}}.
\end{aligned} \tag{19}$$

The final equations of motion for the rotation of the prolate ($\lambda > 1$) ellipsoid particles are given by Euler's equations of rotation presented below in a simplified dimensionless form in Equation (19) [13].

It should be noted that while the hydrodynamic torques in Equation (19) are derived from the Jeffery formulation, which is strictly valid for inertia-free ellipsoids in Stokes flow, they are implemented here within a full rigid-body rotational framework. By solving Euler's equations, we explicitly account for the particle's principal moments of inertia. This ensures that the angular velocity is a predicted state variable rather than an instantaneous function of the local fluid velocity gradient. This approach is consistent with the treatment of translational inertia and provides a reasonable estimate for the low to moderate particle Reynolds numbers observed in this study, where the viscous torque dominates over fluid-inertia-induced torque corrections [13]. Here the elements of the deformation rate tensor ($d_{z'y'}$ and $d_{x'z'}$) and the spin tensor ($\omega_{z'y'}$,$\omega_{x'z'}$, and $\omega_{y'x'}$) are defined as follows:

$$d_{z'y'} = \frac{1}{2}\left(\frac{\partial u_{z'}}{\partial y'} + \frac{\partial u_{y'}}{\partial z'}\right),\ d_{x'z'} = \frac{1}{2}\left(\frac{\partial u_{x'}}{\partial z'} + \frac{\partial u_{z'}}{\partial x'}\right),$$
$$\omega_{z'y'} = \frac{1}{2}\left(\frac{\partial u_{z'}}{\partial y'} - \frac{\partial u_{y'}}{\partial z'}\right),\ \ \omega_{x'z'} = \frac{1}{2}\left(\frac{\partial u_{x'}}{\partial z'} - \frac{\partial u_{z'}}{\partial x'}\right),$$
$$\omega_{y'x'} = \frac{1}{2}\left(\frac{\partial u_{x'}}{\partial y'} - \frac{\partial u_{y'}}{\partial x'}\right). \tag{20}$$

Elements of the deformation-rate tensor and spin tensor are obtained from the transformed velocity gradients:

$$G_{i'j'} = \underline{\underline{\mathbf{A}}} G_{ij} \underline{\underline{\mathbf{A}}}^{-1} \tag{21}$$

The non-dimensional coefficients $\alpha_0 = \beta_0$ , and $\gamma_0$ for a prolate ellipsoid ($\lambda > 1$) are defined as [27]

$$\alpha_0 = \frac{\lambda^2}{\lambda^2 - 1} + \frac{\lambda}{2(\lambda^2-1)^{3/2}} \ln\left(\frac{\lambda - \sqrt{\lambda^2-1}}{\lambda + \sqrt{\lambda^2-1}}\right),$$
$$\gamma_0 = \frac{2}{\lambda^2 - 1} + \frac{\lambda}{(\lambda^2-1)^{3/2}} \ln\left(\frac{\lambda - \sqrt{\lambda^2-1}}{\lambda + \sqrt{\lambda^2-1}}\right). \tag{22}$$

Equations (8)–(10) are advanced in time using a fourth-order Runge–Kutta method, whereas the rotational Equations (19) are integrated using the mixed explicit-implicit scheme of [27] due to their stiffness. The particle solver shares the same time step as the fluid solver.

### 2.2.4 | Coupling

At higher volume fractions, particle–fluid momentum exchange is included via a source term in the Navier–Stokes equations. The acceleration added to fluid cell $i$ is as follows [15]:

$$\mathbf{f}^{*i}_{2W} = \frac{1}{V^*_i} \sum_{j}^{N_{p,i}} \frac{\partial \mathbf{u}^*_{p_j}}{\partial t^*}, \tag{23}$$

where $V^*_i$ is the cell volume and $N_{p,i}$ is the number of particles within the cell. Only contributions from hydrodynamic forces (drag, lift and virtual mass) are included in the acceleration term.

**TABLE 1** | Fixed parameters.

| Fixed parameter | Value |
|---|---|
| Number of particles, $\boldsymbol{N_p}$ | 300000 |
| Particle volume, $\boldsymbol{V^*_p}$ | $6.55 \times 10^{-4}$ |
| Volume fraction, $\boldsymbol{\phi_p}$ | $1.4 \times 10^{-4}$ |
| Shear Stokes number, $\boldsymbol{St^+}$ | 50 |
| Density ratio, $\boldsymbol{\rho^*}$ | 400 |
| Shear Reynolds number, $\boldsymbol{Re_\tau}$ | 300 |
| Bulk Reynolds number, $\boldsymbol{Re_B}$ | 4900 |

Inter-particle collisions are detected using a circumscribed bounding sphere with a radius equal to the particle's semi-major axis. Although this approach simplifies the contact geometry and inherently overestimates the collision cross-section, particularly for the needle-like particles, it serves as a computationally efficient and conservative model for high-inertia interactions. However, as the primary focus of this study is the investigation of translational collision dynamics, this approximation is considered sufficient to capture the dominant physical trends. Future work will look to incorporate more resolved collision models, such as the multi-sphere assembly approach [20], to further refine orientation-dependent interaction statistics. A deterministic binary collision detection method [28] is employed: Particles are binned into a coarse mesh each time step, and potential collisions are identified by examining relative velocities and positions within each cell. A secondary pass identifies missed interactions. Collisions are assumed perfectly elastic and are resolved using conservation of momentum and kinetic energy, with particle positions adjusted to remove overlap.

Particle–wall collisions are treated as perfectly elastic using the same bounding-sphere approximation employed for inter-particle interactions. This restitution-based approach assumes the rebound occurs at the particle centroid, effectively neglecting the torque generated by the lever arm between the actual particle-tip contact point and the center of gravity. Recent high-fidelity modeling [29] indicates that explicitly resolving the particle-wall contact point and the exchange between translational and rotational momentum can significantly alter near-wall orientations and concentrations. However, due to the focus on the translational collision dynamics, and the high particle numbers considered, a computationally efficient simplified model was used.

## 3 | Results and Discussion

We first focus on validation of the model and the collision dynamics of both needle-like (prolate ellipsoids) and near-spherical particles. The fixed parameters for the model are outlined in Table 1. Two volume equivalent particle morphologies are considered with the case specific parameters given in Table 2.

The particles were injected into the domain with random initial position and orientation. The initial velocity was inherited from

**TABLE 2** | Case-specific particle phase parameters.

| Case | $a^*$ | $c^*$ | $\lambda$ |
|---|---|---|---|
| Near-spheres | 0.002492 | 0.002517 | 1.01 |
| Needles | 0.001462 | 0.007310 | 5 |

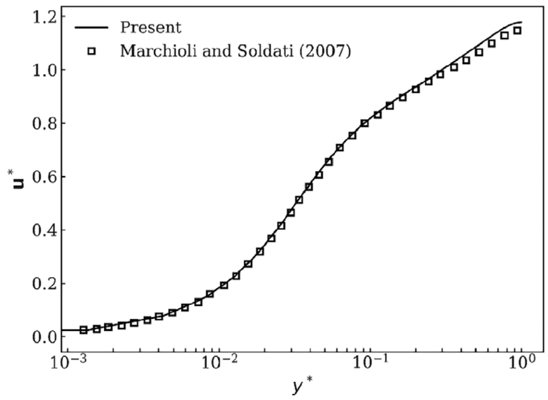


**FIGURE 2** | Profiles of mean fluid streamwise velocity for turbulent channel flow at $Re_\tau = 300$ compared to results from [22].

the fluid, and the initial angular velocity was set to zero. Statistics are reported for the full run-time; transient effects from particle injection were monitored and found to be negligible, with initial condition biases dissipating within a few Stokes time units. Analysis breaks the flows into two distinct regions where the flow conditions are known to differ significantly, namely, the viscous sublayer (VS) ($0 < |y^*| \leq 0.027$), close to the wall where the flow is strongly dominated by shear, and the bulk flow (BF) ($0.2 \leq |y^*| \leq 1.0$), near the channel center where the turbulence is more isotropic. The data of over 1000 binary collisions were collected for each morphology in each region and used to compute collision statistics.

To ensure a rigorous comparison between the different morphologies, the needle-like and near-spherical particles are modeled as volume-equivalent. Given that both cases employ the same material density, the individual particle mass, total solid mass loading, and volume fraction are identical across all simulations. Consequently, any observed differences in turbulence modulation or collision statistics are not artifacts of mass loading but arise solely from the particle shape and the resulting orientation-dependent hydrodynamic forces.

## 3.1 | Validation

### 3.1.1 | Fluid Phase Validation

A single-phase turbulent channel-flow simulation (unladen) was performed to obtain a statistically stationary turbulent flow field at $Re_\tau = 300$. Figures 2 and 3 present the mean streamwise velocity profile, the root-mean-square (RMS) of velocity fluctuations, and the dominant shear stress component. These quantities are compared with the reference data in [30], showing generally good agreement, with only minor deviations observed in the shear stress. This validation confirms the accuracy and

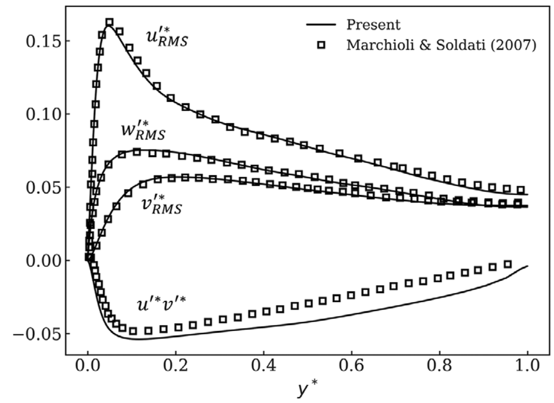


**FIGURE 3** | Profiles of RMS of velocity fluctuations/shear stress for turbulent channel flow at $Re_\tau = 300$ compared to results from [22]. RMS, root-mean-square.

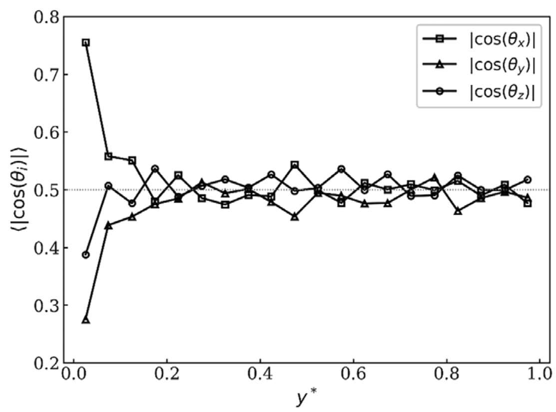


**FIGURE 4** | Profiles of absolute direction cosines for needle-like particles.

reliability of the numerical setup for representing turbulent channel flow.

### 3.1.2 | Orientational Dynamics Validation

Here a one-way coupled multi-phase turbulent channel flow at $Re_\tau = 300$ laden with needle-like particles of aspect ratio $\lambda = 5.0$ (parameters given in Tables 1 and 2) was simulated. We quantify particle alignment by evaluating the cosine of the angles ($\theta_x$,$\theta_y$,$\theta_z$) between the axes of the co-moving frame $x''$ and the particle's principal axis $z'$. These quantities, known as the direction cosines, $\cos(\theta_i)$, provide a measure of how strongly a particle aligns with each axis. Values of $\cos(\theta_i) \approx 1$ indicate strong alignment with axis $i$, whereas $\cos(\theta_i) \approx 0$ indicate little or no alignment. The corresponding probability density functions (PDFs) are obtained using Gaussian kernel density estimation [31].

Figures 4 and 5 quantify the alignment behavior of the needle-like particles. Figure 4 presents the profiles of the absolute mean direction cosines as a function of the wall-normal distance, whereas Figure 5 shows the corresponding absolute direction-cosine PDFs separated by flow region. As shown in Figure 4, particles tend to align with the mean streamwise direction in the near-wall region due to the strong local shear. This alignment

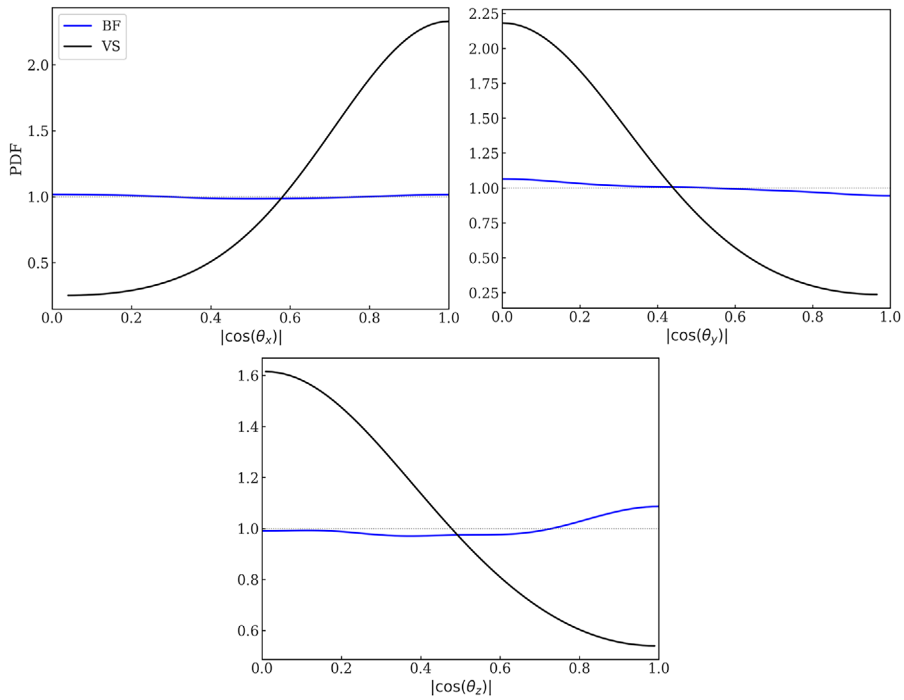


**FIGURE 5** | Absolute direction cosine PDFs by wall normal location for needle-like particles, (left) streamwise alignment, (right) wall normal alignment, and (bottom) spanwise alignment. BF, bulk flow; VS, viscous sublayer; PDFs, probability density functions.

decreases rapidly toward the channel center, where no preferential orientation is observed. This behavior is qualitatively consistent with the observations in [13], where similar simulations were performed for particles with aspect ratio $\lambda = 3$ in a channel flow at $Re_\tau = 150$. The stronger alignment observed in the present study is expected given the larger aspect ratio of our particles.

Figure 5 further supports these trends: strong streamwise alignment is observed within the VS, which diminishes in the BF region. The spanwise and wall-normal components exhibit similar behavior, showing strong anti-alignment with their respective axes near the wall, followed by a progressive weakening toward the channel center. This validation confirms that the particles respond to the local flow conditions as intended and highlights important differences between the flow regions that help explain the variations in collision dynamics observed across our cases.

## 3.2 | Particle Collision Dynamics

Two multiphase turbulent channel-flow simulations were carried out at a shear Reynolds number of $Re_\tau = 300$. The channels were laden with two volume-equivalent particle morphologies representing needle-like particles and near-spherical particles (see Table 2). The relatively high Stokes number of the particles was selected to ensure that the collision behavior is representative of conditions relevant to the nuclear industry. The number of particles, and thus the overall volume fraction, was chosen so that collisions occur frequently and four-way coupling is required to fully capture the collision dynamics. When a collision is detected the code records statistics for each particle which are used to produce PDFs using Gaussian kernel density estimation.

### 3.2.1 | Relative Collision Velocity

The relative collision velocity $|\mathbf{u}_r^*| = \|\mathbf{u}_{p1}^* - \mathbf{u}_{p2}^*\|$, where $\mathbf{u}_{p1}^*$ and $\mathbf{u}_{p2}^*$ are the velocities of particle one and two, respectively, is the magnitude of the difference between the velocity vectors of the particles at the point of collision. Higher values indicate more energetic collision while lower values indicate that the particles are moving more similarly.

Although the relative collision velocity is presented in non-dimensional form, its magnitude is physically significant when compared to the local transport scales. On the basis of the mean streamwise velocity profiles (see Figure 2), the particle velocity $u^*$ peaks at approximately 1.2 in the BF and ranges from roughly 0.0 to 0.6 within the VS.

Figures 6 and 7 show the relative collision velocity PDFs of the near-spherical and needle-like particles in the VS and BF region, respectively. Clear differences between the morphologies are evident. In the VS, the needle-like particles exhibit less variation in relative velocity than the near-spheres. This is directly attributable to the strong streamwise alignment established in the validation phase (see Figure 4), rather than collisional damping as the model employs fully elastic inter particle and wall collisions. As particles align with the local shear, their velocity vectors become more uniform, leading to less energetic interactions. The difference in variance between the two PDFs is smaller in this region because the shear-dominated environment near the wall constrains the motion of both morphologies in a similar way.

In the BF region, the relative velocity is lower because the weak mean shear exposes neighboring particles to more uniform fluid velocities. Here, the variance difference between the morpholo-

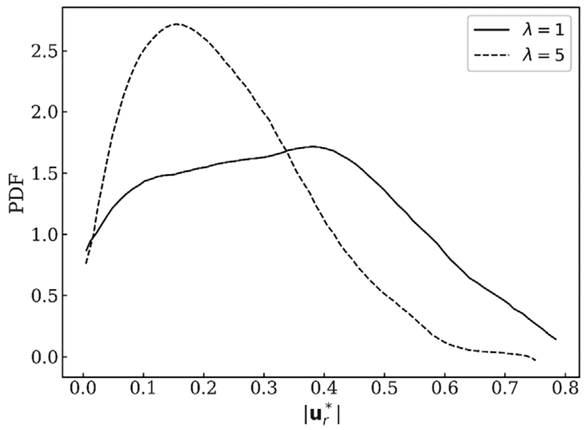


**FIGURE 6** | Collided particle absolute relative velocity PDFs showing collisions in the viscous sublayer. PDFs, probability density functions.

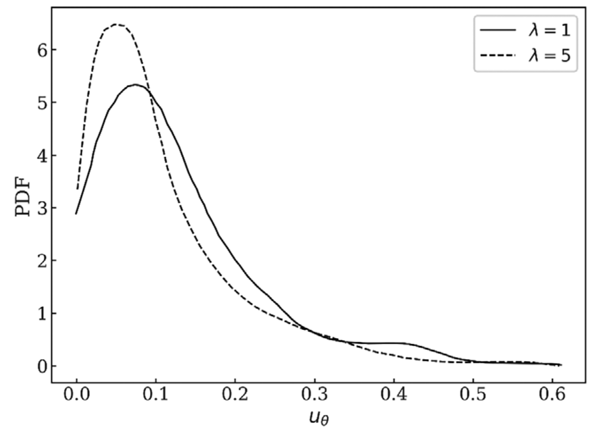


**FIGURE 8** | Collided particle relative collision angle (radians) PDFs showing collisions in the viscous sublayer. PDFs, probability density functions.

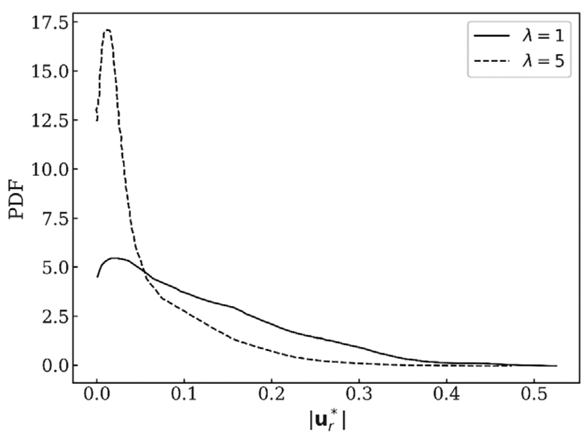


**FIGURE 7** | Collided particle absolute relative velocity PDFs showing collisions in the bulk flow region. PDFs, probability density functions.

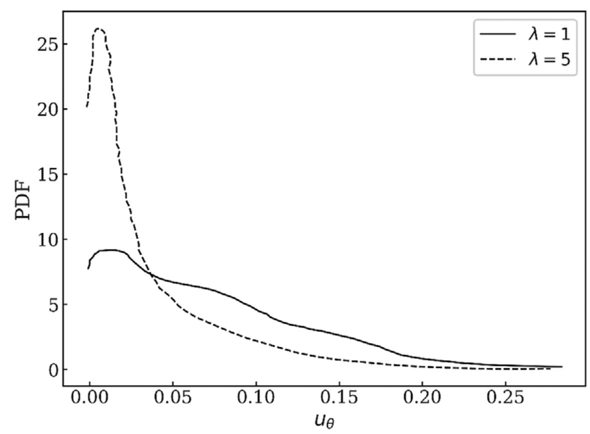


**FIGURE 9** | Collided particle relative collision angle (radians) PDFs showing collisions in the bulk flow region. PDFs, probability density functions.

gies becomes more pronounced. As shown by the direction-cosine PDFs in Figure 5, particles in the BF exhibit more isotropic orientations than those in the VS. However, the needle-like particles still display far less velocity variation than the near-spheres. This may occur because the elongated geometry of the needles provides a filtering effect, where the particle averages the fluid velocity along its major axis, effectively damping the response to small-scale, high-frequency turbulent fluctuations. In contrast, the near-spherical particles lack this orientational stability and are more susceptible to isotropic scattering by the chaotic, small-scale motions present in the BF, leading to the broader relative velocity distributions observed.

### 3.2.2 | Relative Collision Angle

The relative collision angle $u_\theta = \cos^{-1}[(\mathbf{u}^*_{p1} \cdot \mathbf{u}^*_{p2})/\ |\mathbf{u}^*_{p1}||\mathbf{u}^*_{p2}|]$ is the angle between the velocity vectors of colliding particles in radians. High angles (approaching $\pi$) indicate head on collisions while low angles (approaching 0) indicate glancing collisions. Figures 8 and 9 show the relative collision angle PDFs of the near-spherical and needle-like particles in the VS and BF region, respectively.

In the VS, we see a wider spread of collision angles in general when compared to the BF region. This behavior has several potential causes. The strong velocity gradients near the wall cause particles at different wall-normal positions to approach with misaligned velocities. Intermittent sweep and ejection events produce unpredictable particle motions. Finally, collisions with the wall can reflect particle velocities, further increasing the range of relative collision angles. All profiles peak at small values indicating predominantly glancing collisions. This is expected given that the particles are advected through the domain in the streamwise direction which represents the largest component of velocity for all particles.

From Figure 8, we observe similar overall profiles between the different morphologies with slightly less variance observed for the needle-like particles likely due to the strong alignment of elongated particles with the streamwise direction in this region (see Figure 4) and the suppression of wall-normal and spanwise velocity fluctuations arising from strong near-wall shear.

In Figure 9, we see that the relative collision angle of the needle-like particles is more strongly peaked than that of the

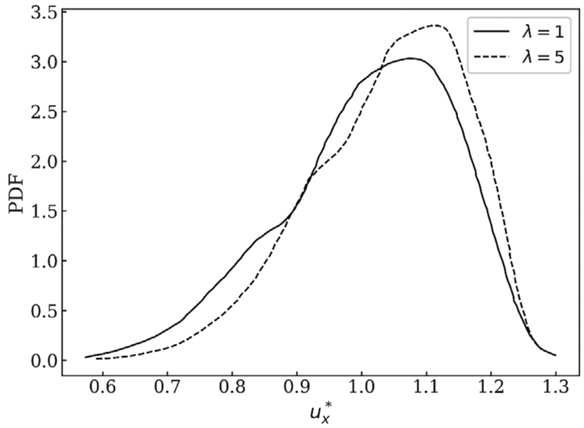


**FIGURE 10** | Collided particle streamwise velocity magnitude PDFs showing collisions in the viscous sublayer. PDFs, probability density functions.

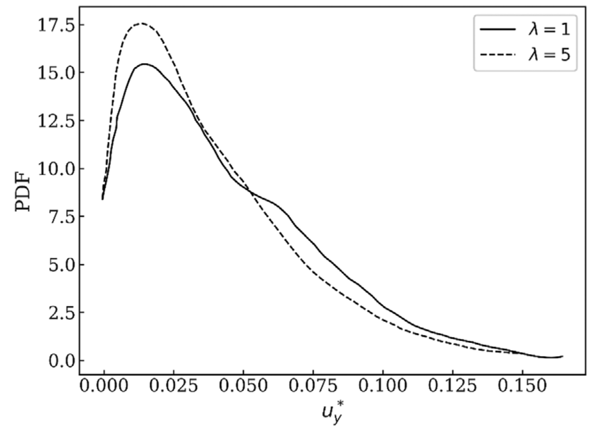


**FIGURE 12** | Collided particle wall-normal velocity magnitude PDFs showing collisions in the viscous sublayer. PDFs, probability density functions.

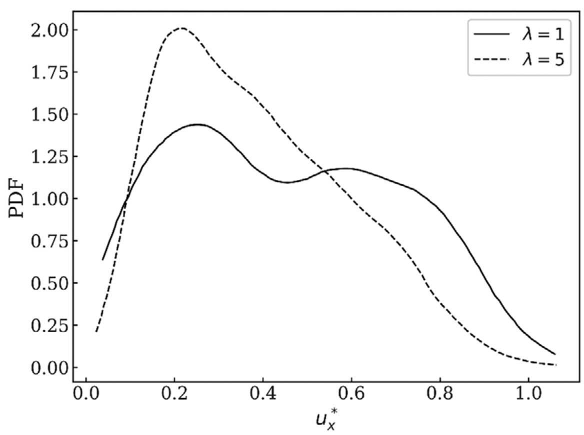


**FIGURE 11** | Collided particle streamwise velocity magnitude PDFs showing collisions in the bulk flow region. PDFs, probability density functions.

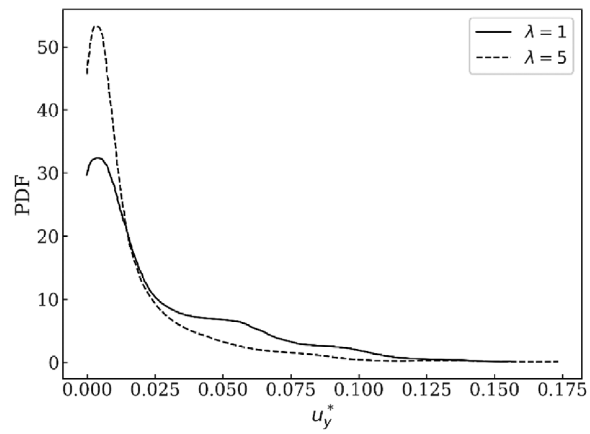


**FIGURE 13** | Collided particle wall-normal velocity magnitude PDFs showing collisions in the bulk flow region. PDFs, probability density functions.

near-spheres in the BF. The reasons for this are largely similar to those for the relative collision velocity. As established by the direction cosines in Figure 5, whereas the BF is more isotropic, the elongated geometry still provides hydrodynamic stability. This makes the needles' trajectories more predictable and aligned with the local flow structures, whereas the near-spheres are more prone to turbulent dispersion, leading to a broader range of approach angles.

### 3.2.3 | Velocity Components

The velocity components of each particle at the time of collision are recorded and used to compute PDFs. All velocity components are generally lower in the VS than the BF region due to the no-slip condition enforced at the walls of the channel making the fluid velocity and thus the particle velocity components smaller.

Figures 10 and 11 show the streamwise component of velocity in the VS and BF region, respectively. The dimensionless velocities $u^*$ follow the bulk-scaled formulation used throughout the simulation. Consequently, the velocity values in the BF (Figure 11) correctly center around 1.2 matching the peak mean transport speed established in the validation phase (Figure 2). Conversely, in the VS (Figure 10), velocities remain below unity as the particles are sampled in the low-momentum region near the wall. In the VS, we see that the streamwise velocity is more variable for the near-spheres, likely because their isotropic shape allows greater response to turbulent fluctuations, whereas needles are stabilized by their strong streamwise alignment with the flow as established in Figure 4. In the BF region, we see similar profiles for both the needles and the near-spheres with slightly higher speeds noted for the needles. One potential reason for this is because their elongated shape promotes alignment with the local flow, reducing dispersion and allowing more efficient motion through turbulent eddies. A notable feature in Figure 10 is the bimodal distribution observed for the near-spherical particles. This bimodality arises as a physical consequence of particles sampling distinct turbulent structures in the VS, namely, low-speed streaks and high-speed sweep events.

Figures 12 and 13 show the wall-normal component of velocity in the VS and the BF region, respectively. The spread of wall-normal velocities is higher in the BF region than in the VS for

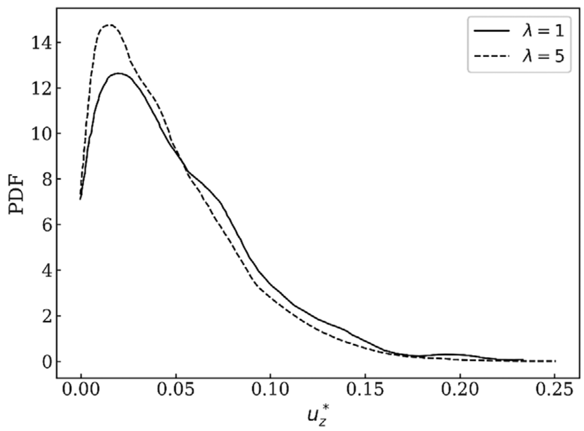


**FIGURE 14** | Collided particle spanwise velocity magnitude PDFs showing collisions in the viscous sublayer. PDFs, probability density functions.

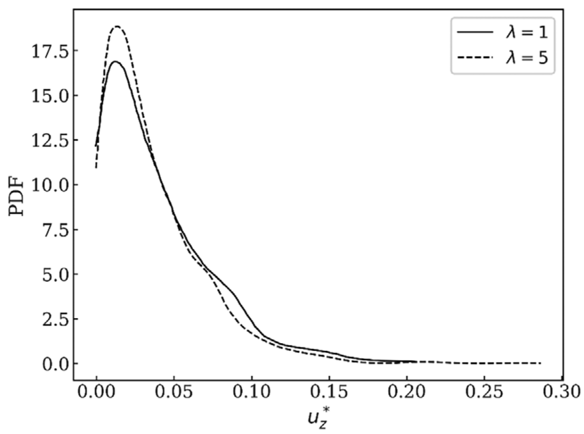


**FIGURE 15** | Collided particle spanwise velocity magnitude PDFs showing collisions in the bulk flow region. PDFs, probability density functions.

both particle morphologies due to the absence of wall constraints and the more isotropic turbulence. Near the walls, the strong shear and no-slip boundary condition suppress such fluctuations, with wall interactions and intermittent sweep and ejection events contributing additional wall-normal motion.

In the VS, we see less variance in the wall-normal velocity for the needle-like particles, a result that is physically consistent with the strong alignment quantified in Section 3.1.2 (Figure 4). Here, the combination of proximity to the wall and the particles' tendency to align with the flow reduces the angle of incidence and thus the lift and drag forces on the needles, resulting in minimal wall-normal velocity fluctuations and the lower variance observed in the PDFs. In the BF region, we see largely similar profiles with slightly less variance for the needle-like particles.

The spanwise velocity is shown in Figures 14 and 15 in the VS and BF region, respectively. We see that regardless of region and morphology the PDFs for spanwise velocity peak around the same values and show similar spreads, with this likely due to the lack of force and walls in this region. We observe that needle-like particles show slightly less variation in the spanwise velocity in both the BF and VS, this is likely resulting from their elongated shape dampening lateral motion when compared to more isotropic morphologies.

## 4 | Conclusions

This work demonstrates that the present numerical framework can reliably capture both fluid turbulence and the particle-flow interactions relevant to high-Stokes number particle-laden flows. Fluid phase predictions agree well with established channel flow simulations, whereas the orientational dynamics confirm that elongated particles respond to shear in a physically consistent manner, exhibiting strong streamwise alignment near the wall and more isotropic behavior in the BF region.

The collision dynamics analysis conducted in this work highlights key differences and similarities between how particles of different aspect ratio collide in various regions of the flow. Needle-like particles experience lower relative collision velocities and less variable collision angle distributions in the BF region. This can be attributed to their enhanced alignment with the local flow and reduced susceptibility to turbulent scattering. Nearly spherical particles on the other hand respond more historically to turbulent fluctuations, producing broader distributions in both collision velocity and angle. Further analysis of the velocity components supports these trends showing that needle-like particles experience damped wall- normal and spanwise fluctuations and more directional motion overall.

Despite these differences, some features are largely morphology independent. Specifically, spanwise velocity statistics are governed by the dominance of turbulent lateral motions rather than particle geometry or collision effects. Overall, these results show that particle shape plays a significant role in collision outcomes, primarily through its influence on alignment and response to shear. These effects become most pronounced in regions where turbulence is strongest and the flow is unconstrained.

Although the present study focuses on the translational kinematics of collisions, which directly dictate the collision energy and approach angles critical for agglomeration modeling, it is recognized that particle shape also exerts a profound influence on rotational dynamics. As demonstrated by [9], particle shape strongly modulates the relative rotation between particles and the surrounding fluid in turbulent channel flows. These rotational fluctuations likely influence the effective collision cross-section and tip-velocities during interactions. Incorporating these shape-dependent rotational statistics represents a natural extension of the present work.

A limitation of the present study is that particle–fluid interactions were represented using reduced-order hydrodynamic closures for drag, lift, and torque rather than fully resolved particle-scale flow simulations. In particular, the translational and rotational dynamics rely on correlations and asymptotic formulations that are most accurate within the low particle Reynolds number regime considered here. Although the adopted models capture the dominant trends in particle alignment and collision kinematics, quantitative predictions may differ for flows involving stronger inertial effects, higher particle

Reynolds numbers, or more complex near-contact hydrodynamic interactions. Nevertheless, the present framework provides a computationally efficient approach for investigating the influence of particle morphology on collision statistics in turbulent channel flows.

---

### Author Contributions

Concept, inception, and strategy: Michael Fairweather, Lee F. Mortimer, and Connor H. Nolan. Model development: Connor H. Nolan, Lee F. Mortimer, and Michael Fairweather. Code development: Connor H. Nolan and Lee F. Mortimer. Results and analysis: Connor H. Nolan, Lee F. Mortimer, and Michael Fairweather. First paper draft: Connor H. Nolan. Review: Lee F. Mortimer, Peter K. Jimack, Connor H. Nolan, and Michael Fairweather. Project guidance: Lee F. Mortimer, Peter K. Jimack, and Michael Fairweather.

### Acknowledgments

The authors would like to thank the EPSRC for funding from the Centre for Doctoral Training in Fluid Dynamics (EP/Y035739/1) and Sellafield Ltd for funding via the Academic Centre of Expertise for Sludge (Particulates and Fluids).

### Conflicts of Interest

The authors declare no conflicts of interest.

### Data Availability Statement

The data that support the findings of this study are available from the corresponding author upon reasonable request.

### References

1. M. A. Allison, B. T. Yuill, E. A. Meselhe, J. K. Marsh, A. S. Kolker, and A. D. Ameen, "Observational and Numerical Particle Tracking to Examine Sediment Dynamics in a Mississippi River Delta Diversion," *Estuarine, Coastal and Shelf Science* 194 (2017): 97–108, https://doi.org/10.1016/j.ecss.2017.06.004.

2. M. Trojanowicz, K. Kołacińska, and J. W. Grate, "A Review of Flow Analysis Methods for Determination of Radionuclides in Nuclear Wastes and Nuclear Reactor Coolants," *Talanta* 183 (2018): 70–82, https://doi.org/10.1016/j.talanta.2018.02.050.

3. F. Lundell, L. D. Söderberg, and P. H. Alfredsson, "Fluid Mechanics of Papermaking," *Annual Review of Fluid Mechanics* 43 (2011): 195–217, https://doi.org/10.1146/annurev-fluid-122109-160700.

4. R. P. J. Kunnen, C. Siewert, M. Meinke, W. Schröder, and K. D. Beheng, "Numerically Determined Geometric Collision Kernels in Spatially Evolving Isotropic Turbulence Relevant for Droplets in Clouds," *Atmospheric Research* 127 (2013): 8–21, https://doi.org/10.1016/j.atmosres.2013.02.003.

5. D. A. Rupp, L. F. Mortimer, and M. Fairweather, "Stokes Number and Coupling Effects on Particle Interaction Behavior in Turbulent Channel Flows," *Physics of Fluids* 35 (2023): 113307, https://doi.org/10.1063/5.0173863.

6. S. Elghobashi, "Direct Numerical Simulation of Turbulent Flows Laden With Droplets or Bubbles," *Annual Review of Fluid Mechanics* 51 (2019): 217–244, https://doi.org/10.1146/annurev-fluid-010518-040401.

7. C. Marchioli, M. Bourgoin, F. Coletti, et al., "Particle-Laden Flows," *International Journal of Multiphase Flow* 191 (2025): 105291, https://doi.org/10.1016/j.ijmultiphaseflow.2025.105291.

8. A. Eshghinejadfard, S. A. Hosseini, and D. Thévenin, "Fully-Resolved Prolate Spheroids in Turbulent Channel Flows: A Lattice Boltzmann Study," *AIP Advances* 7 (2017): 095007, https://doi.org/10.1063/1.5002528.

9. C. Marchioli, L. Zhao, and H. I. Andersson, "On the Relative Rotational Motion Between Rigid Fibers and Fluid in Turbulent Channel Flow," *Physics of Fluids* 28 (2016): 013301, https://doi.org/10.1063/1.4937757.

10. J. R. Fessler, J. D. Kulick, and J. K. Eaton, "Preferential Concentration of Heavy Particles in a Turbulent Channel Flow," *Physics of Fluids* 6 (1994): 3742–3749, https://doi.org/10.1063/1.868445.

11. C. Marchioli and A. Soldati, "Mechanisms for Particle Transfer and Segregation in a Turbulent Boundary Layer," *Journal of Fluid Mechanics* 468 (2002): 283–315, https://doi.org/10.1017/S0022112002001738.

12. L. F. Mortimer, D. O. Njobuenwu, and M. Fairweather, "Near-Wall Dynamics of Inertial Particles in Dilute Turbulent Channel Flows," *Physics of Fluids* 31 (2019): 063302, https://doi.org/10.1063/1.5093391.

13. C. Marchioli, M. Fantoni, and A. Soldati, "Orientation, Distribution, and Deposition of Elongated, Inertial Fibers in Turbulent Channel Flow," *Physics of Fluids* 22 (2010): 033301, https://doi.org/10.1063/1.3328874.

14. G. A. Voth and A. Soldati, "Anisotropic Particles in Turbulence," *Annual Review of Fluid Mechanics* 49, no. 1 (2017): 249–276, https://doi.org/10.1146/annurev-fluid-010816-060135.

15. J. K. Eaton, "Two-Way Coupled Turbulence Simulations of Gas-Particle Flows Using Point-Particle Tracking," *International Journal of Multiphase Flow* 35 (2009): 792–800, https://doi.org/10.1016/j.ijmultiphaseflow.2009.02.009.

16. P. J. Ireland, A. D. Bragg, and L. R. Collins, "The Effect of Reynolds Number on Inertial Particle Dynamics in Isotropic Turbulence. Part 1. Simulations Without Gravitational Effects," *Journal of Fluid Mechanics* 796 (2016): 617–658, https://doi.org/10.1017/jfm.2016.238.

17. C. D. Dritselis, "Direct Numerical Simulation of Particle-Laden Turbulent Channel Flows With Two-and Four-Way Coupling Effects: Budgets of Reynolds Stress and Streamwise Enstrophy," *Fluid Dynamics Research* 48 (2016): 015507, https://doi.org/10.1088/0169-5983/48/1/015507.

18. C. Siewert, R. P. J. Kunnen, and W. Schröder, "Collision Rates of Small Ellipsoids Settling in Turbulence," *Journal of Fluid Mechanics* 758 (2014): 686–701, https://doi.org/10.1017/jfm.2014.554.

19. M. Chen, K. Kontomaris, and J. B. McLaughlin, "Direct Numerical Simulation of Droplet Collisions in a Turbulent Channel Flow. Part I Collision Algorithm," *International Journal of Multiphase Flow* 24 (1999): 1079–1103, https://doi.org/10.1016/S0301-9322(98)00007-X.

20. B. van Wachem, M. Zastawny, F. Zhao, and G. Mallouppas, "Modelling of Gas-Solid Turbulent Channel Flow With Non-Spherical Particles With Large Stokes Numbers," *International Journal of Multiphase Flow* 68 (2015): 80–92.

21. P. F. Fischer, J. W. Lottes, and S. G. Kerkemeier, Nek5000: Open Source Spectral Element CFD Solver [Computer Software], (Argonne National Laboratory, 2008), Available at: http://nek5000.mcs.anl.gov/.

22. C. Yin, L. Rosendahl, S. K. Kær, and H. Sørensen, "Modelling the Motion of Cylindrical Particles in a Nonuniform Flow," *Chemical Engineering Science* 58 (2003): 3489–3498, https://doi.org/10.1016/S0009-2509(03)00214-8.

23. G. H. Ganser, "A Rational Approach to Drag Prediction of Spherical and Nonspherical Particles," *Powder Technology* 77 (1993): 143–152, https://doi.org/10.1016/0032-5910(93)80051-B.

24. M. Zastawny, G. Mallouppas, F. Zhao, and B. Van Wachem, "Derivation of Drag and Lift Force and Torque Coefficients for Non-Spherical Particles in Flows," *International Journal of Multiphase Flow* 39 (2012): 227–239, https://doi.org/10.1016/j.ijmultiphaseflow.2011.09.004.

25. R. Ouchene, M. Khalij, A. Tanière, and B. Arcen, "Drag, Lift and Torque Coefficients for Ellipsoidal Particles: From Low to Moderate Particle Reynolds Numbers," *Computers & Fluids* 113 (2015): 53–64, https://doi.org/10.1016/j.compfluid.2014.12.005.

26. V. Chéron, F. Evrard, and B. van Wachem, "Drag, Lift and Torque Correlations for Axi-Symmetric Rod-Like Non-Spherical Particles in Locally Linear Shear Flows," *International Journal of Multiphase Flow* 171 (2024): 104692.

27. F. G. Fan and G. Ahmadi, "A Sublayer Model for Wall Deposition of Ellipsoidal Particles in Turbulent Streams," *Journal of Aerosol Science* 26 (1995): 813–840, https://doi.org/10.1016/0021-8502(95)00021-4.

28. M. Breuer and N. Almohammed, "Modeling and Simulation of Particle Agglomeration in Turbulent Flows Using a Hard-Sphere Model With Deterministic Collision Detection and Enhanced Structure Models," *International Journal of Multiphase Flow* 73 (2015): 171–206, https://doi.org/10.1016/j.ijmultiphaseflow.2015.03.018.

29. M. A. Taborda and M. Sommerfeld, "Effect of Wall-Collision Models on the Transport of Rigid, Elongated Non-Spherical Particles in a Turbulent Channel Flow Using an Euler/Lagrange Approach," *Computers & Fluids* 306 (2025): 106940.

30. C. Marchioli and A. Soldati, "Reynolds Number Scaling of Particle Preferential Concentration in Turbulent Channel Flow," in *Advances in Turbulence XI* (Springer, 2007), https://doi.org/10.1007/978-3-540-72604-3.

31. M. Rosenblatt, "Remarks on Some Nonparametric Estimates of a Density Function," *Annals of Mathematical Statistics* 27, no. 3 (1956): 832–837, https://doi.org/10.1214/aoms/1177728190.

32. R. Ouchene, M. Khalij, B. Arcen, and A. Tanière, "A New Set of Correlations of Drag, Lift and Torque Coefficients for Non-Spherical Particles and Large Reynolds Numbers," *Powder Technology* 303 (2016): 33–43, https://doi.org/10.1016/j.powtec.2016.07.067.


### Appendix A: Particle Reynolds Number and Model Applicability

The particle Reynolds number $Re_p$ was evaluated to access the validity of the drag and rotational models employed in the present study. The probability density function of $Re_p$ obtained from our simulations is shown in Figure A1. The average particle Reynolds number was found to be approximately $Re_p \approx 1.0$, with the majority of particles remaining within the low-Reynolds-number regime.

The particle Reynolds numbers observed within the present simulations are consistent with the range of applicability of both the Ganser drag correlation [23] and Jeffery's rotational formulation. Comparisons were performed against DNS data and the empirical correlations reported in [32]. In particular, the Ganser drag correlation was compared with the correlation proposed by Ouchene et al. for the specific case of $Re_p = 1.21$ and particle aspect ratio $\lambda = 1.25$. This case was selected as it is representative of the parameter range encountered in the present simulations

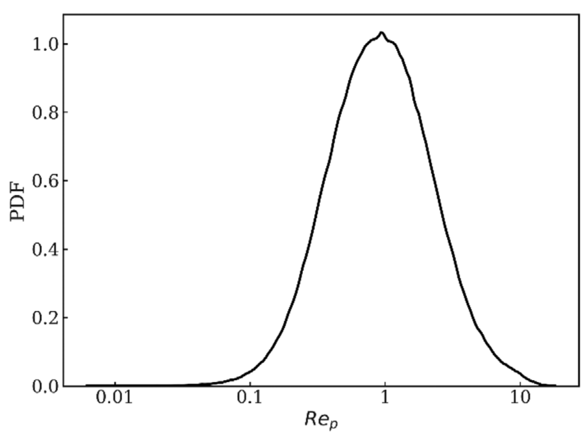


**FIGURE A1** | PDF of particle Reynolds number observed in non-spherical turbulent channel flow simulations. PDFs, probability density functions.

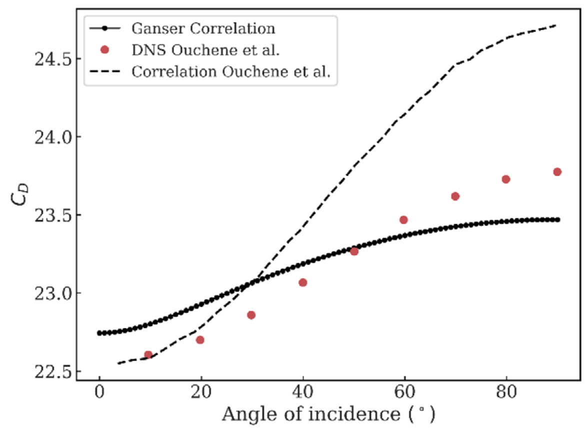


**FIGURE A2** | Comparison of drag coefficients observed from Ganser drag correlation [23] and Ouchene et al. [32] over angles of incidence. Correlations are compared to outputs obtained from fully resolved DNS simulations. DNS, direct numerical simulation.

This comparison can be seen in Figure A2. The Ganser correlation captures the overall trend of the drag coefficient with increasing angles of incidence, showing good agreement with DNS results at intermediate angles. Although more accurate at lower angles of incidence the Ouchene correlation begins to overpredict the drag coefficient compared to the DNS at higher angles. Within this low particle Reynolds number regime, it is therefore preferable to employ the Ganser formulation due to its stable behavior across the entire range of orientations and its lower average error.